

Density wave and topological superconductivity in the magic-angle-twisted bilayer-graphene

Ming Zhang(张铭)[1], Yu Zhang(张渝)[2], Chen Lu(卢晨)[1], Wei-Qiang Chen(陈伟强)[2,†], and and Fan Yang(杨帆)[1,‡]

Citation: Chin. Phys. B, 2020, 29 (**12**): 127102. DOI: 10.1088/1674-1056/abc7b5
Journal homepage: http://cpb.iphy.ac.cn; http://iopscience.iop.org/cpb

What follows is a list of articles you may be interested in

Benchmarking the simplest slave-particle theory with Hubbard dimer

Wei-Wei Yang(杨薇薇), Hong-Gang Luo(罗洪刚), Yin Zhong(钟寅)
Chin. Phys. B, 2019, 28 (**10**): 107103. DOI: 10.1088/1674-1056/ab3dfe

Hubbard model on an anisotropic checkerboard lattice at finite temperatures: Magnetic and metal-insulator transitions

Hai-Di Liu(刘海迪)
Chin. Phys. B, 2019, 28 (**10**): 107102. DOI: 10.1088/1674-1056/ab4279

Electronic structure from equivalent differential equations of Hartree-Fock equations

Hai Lin(林海)
Chin. Phys. B, 2019, 28 (**8**): 087101. DOI: 10.1088/1674-1056/28/8/087101

Phase diagram, correlations, and quantum critical point in the periodic Anderson model

Jian-Wei Yang(杨建伟), Qiao-Ni Chen(陈巧妮)
Chin. Phys. B, 2018, 27 (**3**): 037101. DOI: 10.1088/1674-1056/27/3/037101

Novel high-*K* with low specific on-resistance high voltage lateral double-diffused MOSFET

Li-Juan Wu(吴丽娟), Zhong-Jie Zhang(章中杰), Yue Song(宋月), Hang Yang(杨航), Li-Min Hu(胡利民), Na Yuan(袁娜)
Chin. Phys. B, 2017, 26 (**2**): 027101. DOI: 10.1088/1674-1056/26/2/027101

SPECIAL TOPIC — Twistronics

Density wave and topological superconductivity in the magic-angle-twisted bilayer-graphene*

Ming Zhang(张铭)[1], Yu Zhang(张渝)[2], Chen Lu(卢晨)[1], Wei-Qiang Chen(陈伟强)[2,†], and Fan Yang(杨帆)[1,‡]

[1] School of Physics, Beijing Institute of Technology, Beijing 100081, China

[2] Institute for Quantum Science and Engineering and Department of Physics, Southern University of Science and Technology, Shenzhen 518055, China

(Received 29 May 2020; revised manuscript received 21 September 2020; accepted manuscript online 5 November 2020)

The model dependence in the study of the magic-angle twisted bilayer-graphene (MA-TBG) is an important issue in the research area. It has been argued previously that the two-band tight-binding (TB) model (per spin and valley) cannot serve as a start point for succeeding studies as it cannot correctly describe the topological aspect of the continuum-theory model near the Dirac nodes in the mini Brillouin zone (MBZ). For this purpose, we adopt the faithful TB model [*Phys. Rev. B* **99** 195455 (2019)] with five bands (per spin and valley) as our start point, which is further equipped with extended Hubbard interactions. Then after systematic random-phase-approximation (RPA) based calculations, we study the electron instabilities of this model, including the density wave (DW) and superconductivity (SC), near the van Hove singularity (VHS). Our results are as follows. In the case neglecting the tiny inter-valley exchange interaction, the exact $SU(2)_K \times SU(2)_{K'}$ symmetry leads to the degeneracy between the inter-valley charge DW (CDW) and the spin DW (SDW) (which would be mixed then), and that between the singlet $d+id$-wave and triplet $p+ip$-wave topological SCs. When a realistic tiny inter-valley exchange interaction is turned on with nonzero coefficient ($J_H \neq 0$), the SDW or CDW is favored respectively at the critical point, determined by $J_H \to 0^-$ or $J_H \to 0^+$. In the mean time, the degeneracy between the singlet $d+id$-wave and triplet $p+ip$-wave topological SCs is also lifted up by the tiny J_H. These results are highly similar to the results of our previous study [arXiv:2003.09513] adopting the two-band TB model, with the reason lying in that both models share the same symmetry and Fermi-surface (FS) nesting character near the VHS. Such a similarity suggests that the low-energy physics of the doped MA-TBG is mainly determined by the symmetry and the shape of the FS of the doped system, and is insensitive to other details of the band structure, including the topological aspects near the Dirac nodes in the MBZ.

Keywords: magic-angle twisted bilayer-graphene (MA-TBG), van Hove singularity (VHS), density wave (DW), pairing symmetries

PACS: 71.10.–w, 74.25.Dw, 81.05.ue **DOI:** 10.1088/1674-1056/abc7b5

1. Introduction

The synthesization of the magic-angle twisted bilayer-graphene (MA-TBG) is one of the major breakthroughs in condensed matter physics since 2018,[1,2] Its special Moiré structure[3–19] causes a greatly enlarged unit cell and thousands of energy bands formed in the mini Brillouin zone (MBZ). Notably, the nearly flat bands containing Dirac nodes bring about strong electron correlations and various types of electron instabilities, including the correlated insulators and superconductivity (SC). Now the nature of the correlated insulator,[2,20–48] pairing mechanism, and pairing symmetry[1,36–73] are still under debate. In our work, we adopt the weak-coupling point of view first proposed by two of the present authors in Ref. [38] that the electron instabilities of the MA-TBG, including the correlated insulator and SC, are driven by the Fermi-surface (FS) nesting near the van Hove singularity (VHS). This point of view is followed by various research groups.[45–48,68–70,74–78]

In the weak-coupling framework, an important issue was first proposed in Refs. [47,48]: due to the approximate $SU(2)_K \times SU(2)_{K'}$ symmetry of the MA-TBG, the inter-valley charge density wave (CDW) and spin density wave (SDW) are nearly degenerate, so do the singlet SC and triplet one. However, no serious study on the form of the ground-state order parameters of the density wave (DW) and SC was performed until our recent work[79] which suggests that the mixing of the CDW and SDW at the exactly symmetric point would lead to a novel DW state dubbed as the chiral SO(4) spin–charge DW. This DW state simultaneously hosts three mutually perpendicular 4-component vectorial spin–charge DW order parameters which can globally arbitrarily rotate in the $\mathbb{R}^4$ space without costing energy. When a tiny $SU(2)_K \times SU(2)_{K'}$-symmetry-breaking inter-valley exchange interaction turns on, the chiral SO(4) DW order can decay into either a pure SDW or a nematic DW state with mixed stripy CDW and SDW orders, determined by the sign of the coefficient of the exchange in-

*Project supported by the National Natural Science Foundation of China (Grant Nos. 11674025, 12074031, and 11674151) and the National Key Research and Development Program of China (Grant No. 2016YFA0300300).

†Corresponding author. E-mail: chenwq@sustech.edu.cn

‡Corresponding author. E-mail: yangfan_blg@bit.edu.cn

© 2020 Chinese Physical Society and IOP Publishing Ltd

teraction. On the other hand, the degenerate triplet $p+ip$ and singlet $d+id$ pairing symmetries would decay into pure $p+ip$ or $d+id$.

There is a problem with respect to the TB model adopted in our recent work.[79] In that work, we adopt the two-band (per spin and valley) TB model on the honeycomb lattice introduced in Refs. [35,80]. This model is criticized to be topologically problematic: As the two Dirac points in the mini BZ originate from the same valley of the unperturbed layers, they should carry the same chirality. However, any two-band TB model would give opposite chiralities for the two Dirac points. Therefore, only more complicated band structure can capture this topology. Here we adopt the five-band (per spin and valley) TB model first proposed in Ref. [81]. This model can capture both the symmetry and topology aspects of the continuum-theory model, and can thus serve as a faithful TB model of the MA-TBG. Local Hubbard-like interactions are then added to this five-band model, leading to an extended Hubbard model, which provides the start point of our study.

In this paper, we study the extended Hubbard model containing the five-band TB model proposed in Ref. [81] as its kinetic part. With standard multi-orbital RPA approach, we study both the DW instabilities and pairing symmetry of the MA-TBG. Our results reveal that both the DW and the SC in the system belong to inter-valley type of orders. At the exact $SU(2)_K \times SU(2)_{K'}$-symmetric point with no inter-valley exchange interaction, our RPA results reveal that the critical interaction strengths U_c for the SDW and CDW orders are equal, i.e., $U_c^{(c)} = U_c^{(s)}$, suggesting that these two DW orders are degenerate at the critical point. Such a degeneracy at the critical point is lifted up by an infinitesimal symmetry-breaking inter-valley exchange interaction with the coefficient J_H. When $J_H \to 0^-$, we get $U_c^{(c)} > U_c^{(s)}$, suggesting that the SDW order is more easily formed than the CDW. When $J_H \to 0^+$, we get $U_c^{(c)} < U_c^{(s)}$, suggesting that the CDW order is preferred. The situation for the SC is similar. At the symmetric point with $J_H = 0$, we obtain degenerate triplet $p+ip$[82] and singlet $d+id$, which decay into one of the two when a tiny J_H turns on. The results obtained here are similar with those obtained for the two-band Hubbard model which we studied previously.[79]

The rest of this paper is organized as follows. In Section 2, we describe the adopted model and approach. In Section 3, we analyze the results of numerical calculations: we study the case of $J_H = 0$ in which the system hosts the exact $SU(2)_K \times SU(2)_{K'}$ symmetry and reinvestigate the problem in tiny $J_H \neq 0$, including the cases $J_H = 0^+$ and $J_H = 0^-$. Finally, in Section 4, conclusions are reached with further discussions.

2. Model and approach

2.1. Model

There are four low-energy flat bands (for each spin) near the Fermi level of the MA-TBG, which are well isolated from the high-energy bands.[4,25,31,35,51,52,83] Since the band structure originating from the two valleys that are related by the time-reversal symmetry (TRS),[3,84] we are allowed to provide a band structure containing two low-energy flat bands for one valley, and the remaining energy bands for the other valley can be obtained by the TRS. We choose a five-band model[81] for one valley and spin which can faithfully reproduces the features of the TBG bands in the energy window from roughly -100 meV to the top of the two nearly flat bands and it will capture all the energetic, symmetry, and topological features of the two nearly flat bands in TBG.

The model is constructed on a honeycomb lattice,[81] as shown in Fig. 1(a). On the center of each hexagon (as represented by the yellow circle) on the lattice, there exist three orbitals for each valley and spin, which possess the p_z, p_+, and p_- symmetries, respectively. On each lattice site (the green circle), there exists an s-orbital. As we have two sublattices on the honeycomb lattice, the two s-wave orbitals represent two different effective orbitals. Altogether, we have three p-wave orbitals locating at the same point, and two s-wave orbitals locating at two different points within each unit cell, forming the 5 effective orbitals for each valley and spin.

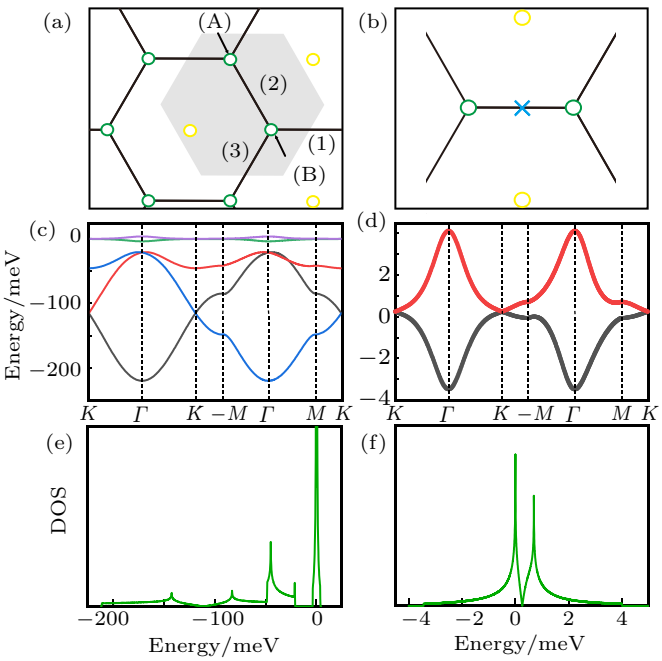


Fig. 1. The lattice structure for the five-band (per valley and spin) TB model representing the MA-TBG, and the corresponding band structure for the valley K. (a) The lattice structure. On the center of each hexagon (yellow circle), there exist three orbitals with p_z, p_+, and p_- symmetries, respectively. On each lattice site (green circle), there exists an s-orbital. (b) At the middle point of each nearest-neighbor bond on the honeycomb lattice, the cross represents the center of a quasi orbital. These crosses form a Kagome lattice. (c) The band structure (for the valley K) of the five-band TB model. (d) Low-energy broadening of (c), with the two flat bands singled out. (e) The DOS of the band structure shown in (c). (f) The low-energy broadening of (e), contributed only by the two flat bands. Two VHS points are present, with the one in the negative band denoted as h-VHS and the one in the positive band denoted as e-VHS.

The effective 5-band TB model for one valley, say the valley K, is as follow:

$$\hat{H}_{\rm TB}^{\rm (K)} = \sum_{\boldsymbol{k}\iota_1\iota_2\sigma} c^{\dagger}_{\boldsymbol{k}{\rm K}\iota_1\sigma} h^{\rm K}_{\iota_1\iota_2}(\boldsymbol{k}) c_{\boldsymbol{k}{\rm K}\iota_2\sigma}. \tag{1}$$

Here $c^{\dagger}_{\boldsymbol{k}{\rm K}\iota\sigma}$ ($c_{\boldsymbol{k}{\rm K}\iota\sigma}$) creates (annihilates) an electron at the valley K with momentum $\boldsymbol{k}$, orbital ι, and spin σ. Here $\iota = 1,\ldots,5$ represent the five effective orbitals, with $\iota = 1,2,3$ representing the p_z, p_+, and p_- orbitals locating on the center of each hexagon, and $\iota = 4,5$ representing the s-wave orbitals locating on the A and B sublattices, respectively. The 5×5 matrix $h^{\rm K}(\boldsymbol{k})$ with its entries $h^{\rm K}_{\iota_1\iota_2}(\boldsymbol{k})$ is given as[81]

$$h^{\rm K}(\boldsymbol{k}) = -t_0'\rho_{\boldsymbol{k}}\rho^{\dagger}_{\boldsymbol{k}} + {\rm diag}(\varepsilon_{p_z},\varepsilon_{p_\pm},\varepsilon_{p_\pm},\varepsilon_\eta,\varepsilon_\eta). \tag{2}$$

Here ε_μ represents the chemical potential for the effective orbital μ. The $\rho_{\boldsymbol{k}} \equiv (\rho^{(1)}_{\boldsymbol{k}},\rho^{(2)}_{\boldsymbol{k}},\rho^{(3)}_{\boldsymbol{k}})$, and the three $\rho^{(l)}_{\boldsymbol{k}}(l = 1,2,3)$ column vectors are defined as[81]

$$\rho^{(1)}_{\boldsymbol{k}} = \begin{pmatrix} {\rm i}\tilde{a}(\phi_{11}-\phi_{10}) \\ \tilde{b}\,\phi_{11}+\tilde{c}\,\phi_{10} \\ \tilde{c}\,\phi_{11}+\tilde{b}\,\phi_{10} \\ \tilde{d}^*\phi_{10} \\ \tilde{d} \end{pmatrix};$$

$$\rho^{(2)}_{\boldsymbol{k}} = \begin{pmatrix} {\rm i}\tilde{a}(1-\phi_{11}) \\ \omega(\tilde{b}+\tilde{c}\,\phi_{11}) \\ \omega^*(\tilde{c}+\tilde{b}\,\phi_{11}) \\ \tilde{d}^* \\ \tilde{d} \end{pmatrix};$$

$$\rho^{(3)}_{\boldsymbol{k}} = \begin{pmatrix} {\rm i}\tilde{a}(\phi_{10}-1) \\ \omega^*(\tilde{b}\,\phi_{10}+\tilde{c}) \\ \omega(\tilde{c}\,\phi_{10}+\tilde{b}) \\ \tilde{d}^*\phi_{0\bar{1}} \\ \tilde{d} \end{pmatrix}, \tag{3}$$

where $\tilde{a}$, $\tilde{b}$, $\tilde{c}$ are real, $\tilde{d}$ can be complex, and $\phi_{lm} \equiv {\rm e}^{-{\rm i}\boldsymbol{k}\cdot(l\boldsymbol{a}_1+m\boldsymbol{a}_2)}$.

On the above, the l-index for the column vector $\rho^{(l)}_{\boldsymbol{k}}$ originates from the three quasi-orbital Fermion states, with each centering at the middle point of each nearest-neighbor bond on the honeycomb lattice, as shown by the cross point in Fig. 1(b). The band structure thus obtained is shown in Fig. 1(c), with the broadened two low-energy flat bands shown in Fig. 1(d). The obtained band structure is well consistent with that of the continuum-model[3] in the aspect of symmetry representation and topology.[81] The obtained density of state (DOS) of the band structure is shown in Fig. 1(e), with its low-energy broadened DOS for the two flat bands shown in Fig. 1(f). From Fig. 1(f), one verifies the presence of two VHS points in the low-energy band structure, with the one in the negative band defined as h-VHS and the one in the positive band defined as e-VHS.

The effective TB Hamiltonian for the other valley K′ is obtained from that for the valley K through a TRS as follows:

$$\hat{H}_{\rm TB}^{\rm (K')} = \sum_{\boldsymbol{k}\iota_1\iota_2\sigma} c^{\dagger}_{\boldsymbol{k}{\rm K}'\iota_1\sigma} h^{\rm K'}_{\iota_1\iota_2}(\boldsymbol{k}) c_{\boldsymbol{k}{\rm K}'\iota_2\sigma}, \tag{4}$$

with

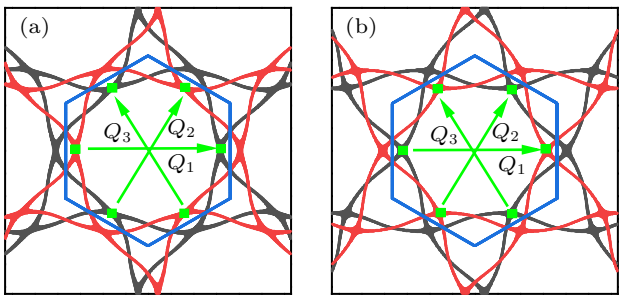
$$h^{\rm K'}(\boldsymbol{k}) = (h^{\rm K}(-\boldsymbol{k}))^*. \tag{5}$$

The total TB Hamiltonian for the system is thus

$$\begin{aligned}\hat{H}_{\rm TB} &= \hat{H}_{\rm TB}^{\rm (K)} + \hat{H}_{\rm TB}^{\rm (K')} \\ &\equiv \sum_{v_1\iota_1 v_2\iota_2\boldsymbol{k}\sigma} c^{\dagger}_{\boldsymbol{k}v_1\iota_1\sigma} h_{v_1\iota_1,v_2\iota_2}(\boldsymbol{k}) c_{\boldsymbol{k}v_2\iota_2\sigma},\end{aligned} \tag{6}$$

with $\iota = \{1,2,3,4,5\}$ representing the orbital index and $v = \pm$ denoting the K and K' valleys . The 10×10 matrix $h(\boldsymbol{k})$ is the direct sum of $h^{\rm K}(\boldsymbol{k})$ and $h^{\rm K'}(\boldsymbol{k})$, i.e., $h(\boldsymbol{k}) = h^{\rm K}(\boldsymbol{k}) \oplus h^{\rm K'}(\boldsymbol{k})$.

The FSs at the h-VHS and e-VHS doping levels with $\delta = -0.225$ and 0.305 are shown in Figs. 2(a) and 2(b), respectively. Note that each valley will contribute a FS, and the black and red curves correspond to the FSs from the K and K′ valleys, respectively. The FSs shown in both Figs. 2(a) and 2(b) exhibit good nesting, with the three FS-nesting vectors in green denoted as $\boldsymbol{Q}_\alpha$. Such good FS-nesting implies the formation of DW and SC when interactions turn on in the system.



FS at h-VHS point FS at e-VHS point

Fig. 2. (a) and (b) FSs at the h-VHS and e-VHS doping levels with $\delta = -0.225$ and 0.305, respectively. The blue hexagon represents the MBZ. The black and red curves correspond to the FSs from the K and K' valleys, respectively. The three $\boldsymbol{Q}_\alpha$ in green mark the FS-nesting vectors.

The interaction part of the Hamiltonian is

$$\begin{aligned}\hat{H}_{\rm int} &= U\sum_{\substack{i\\ v\iota\in D}} \hat{n}_{iv\iota\uparrow}\hat{n}_{iv\iota\downarrow} + U\sum_{\substack{i\sigma\sigma'\\ v_1\iota_1<v_2\iota_2\in D}} \hat{n}_{iv_1\iota_1\sigma}\hat{n}_{iv_2\iota_2\sigma'} \\ &+ U'\sum_{\substack{i\\ v\iota\in D'}} \hat{n}_{iv\iota\uparrow}\hat{n}_{iv\iota\downarrow} \\ &+ U'\sum_{\substack{i\sigma\sigma'\\ v_1\iota_1<v_2\iota_2\in D'}} \hat{n}_{iv_1\iota_1\sigma}\hat{n}_{iv_2\iota_2\sigma'}\delta_{v_1\iota_1,v_2\iota_2-5} \\ &+ W\sum_{\substack{\langle i,j\rangle,\sigma,\sigma'\\ v_1\iota_1\in(4,9)\\ v_2\iota_2\in(5,10)}} \hat{n}_{iv_1\iota_1\sigma}\hat{n}_{jv_2\iota_2\sigma'} \\ &- J_{\rm H}\sum_{\substack{i\sigma\sigma'\\ v\iota\in D}} \hat{c}^{\dagger}_{iv\iota\sigma}\hat{c}_{i\bar{v}\iota\sigma}\hat{c}^{\dagger}_{i\bar{v}\iota\sigma'}\hat{c}_{iv\iota\sigma'},\end{aligned} \tag{7}$$

where $\hat{n}_{iv\iota\sigma} = \hat{c}^{\dagger}_{iv\iota\sigma}\hat{c}_{iv\iota\sigma}$, $D = [1,2,3,6,7,8]$, $D' = [4,5,9,10]$, labelling orbitals combined with valley $\{\tau_{p_z;+},\tau_{p_+;+},\tau_{p_-;+},\eta^{(A)}_{s;+},\eta^{(B)}_{s;+},\tau_{p_z;-},\tau_{p_+;-},\tau_{p_-;-},\eta^{(A)}_{s;-},\eta^{(B)}_{s;-},\}$ as $\{1,2,3,\cdots,9,10\}$, v and $\bar{v}$ stand for the opposite valleys.

The first (second) two terms represent the intra-orbital and inter-orbital Hubbard interactions between the p-wave (s-wave) orbitals, which have equal coefficients.[80] Physically, the Hubbard interactions between the p-wave orbitals are usually stronger than those between the s-wave ones. So, we have $U' < U$. In our calculations, we adopt $U' = U/2$. The W-term represents the nearest-neighbor density–density interaction between the s-wave orbitals, with its coefficient $W \approx U'/3$, due to the extended property of the Wannier wave functions shown in Figs. 1(a) and 1(b). The tiny inter-valley Hund's-rule exchange interaction is given by the last term with the strength $J_{\rm H}$ two orders of magnitude weaker than U.[85] The total Hamiltonian of the system is given by

$$\hat{H} = \hat{H}_{\rm TB} + \hat{H}_{\rm int}. \tag{8}$$

While the TB part and the dominant interactions in this Hamiltonian possess the $\mathrm{SU(2)_K \times SU(2)_{K'}}$ symmetry, a tiny inter-valley exchange interaction breaks it. Besides, the model holds a D_3 symmetry, which leads to three degenerate FS-nesting vectors $\boldsymbol{Q}_\alpha$ ($\alpha = 1,2,3$) near the VHS points, as shown in Figs. 2(a) and 2(b).

2.2. The PRA approach

The RPA approach is used in this work to study the electron instabilities driven by the FS-nesting and VHS. According to the standard multi-orbital RPA approach,[86–95] the following bare susceptibility is defined for the non-interacting case:

$$\chi^{(0)l_1l_2}_{l_3l_4}(\boldsymbol{q},\tau) \equiv \frac{1}{N}\sum_{\boldsymbol{k}_1\boldsymbol{k}_2}\left\langle T_\tau \hat{c}^\dagger_{\boldsymbol{k}_1 l_1\sigma}(\tau)\hat{c}_{\boldsymbol{k}_1+\boldsymbol{q}l_2\sigma}(\tau)\ \hat{c}^\dagger_{\boldsymbol{k}_2+\boldsymbol{q}l_4\sigma}(0)\hat{c}_{\boldsymbol{k}_2 l_3\sigma}(0)\right\rangle_0, \tag{9}$$

where $\boldsymbol{q}$ and $\boldsymbol{k}_{1,2}$ are the wave vectors, $l_{1,\cdots,4} = (\nu\iota)$ with $\iota = \{1,2,3,4,5\}$ represents the orbital index, and $\nu = \pm$ denotes the K and K′ valleys, respectively. The $\langle\cdots\rangle_0$ denotes the thermal average of the noninteracting system. The explicit formula of $\chi^{(0)l_1l_2}_{l_3l_4}(\boldsymbol{q},\tau)$ is given in Appendix A.

When interactions are turned on, we define the following renormalized spin and charge susceptibilities:

$$\chi^{(\mathrm{s})l_1l_2}_{l_3l_4}(\boldsymbol{q},\tau) \equiv \frac{1}{2N}\sum_{\boldsymbol{k}_1\boldsymbol{k}_2,\sigma_1\sigma_2}\left\langle T_\tau \hat{c}^\dagger_{\boldsymbol{k}_1 l_1\sigma_1}(\tau)\hat{c}_{\boldsymbol{k}_1+\boldsymbol{q}l_2\sigma_1}(\tau) \times \hat{c}^\dagger_{\boldsymbol{k}_2+\boldsymbol{q}l_4\sigma_2}(0)\hat{c}_{\boldsymbol{k}_2 l_3\sigma_2}(0)\right\rangle \sigma_1\sigma_2, \tag{10a}$$

$$\chi^{(\mathrm{c})l_1l_2}_{l_3l_4}(\boldsymbol{q},\tau) \equiv \frac{1}{2N}\sum_{\boldsymbol{k}_1\boldsymbol{k}_2,\sigma_1\sigma_2}\left\langle T_\tau \hat{c}^\dagger_{\boldsymbol{k}_1 l_1\sigma_1}(\tau)\hat{c}_{\boldsymbol{k}_1+\boldsymbol{q}l_2\sigma_1}(\tau) \times \hat{c}^\dagger_{\boldsymbol{k}_2+\boldsymbol{q}l_4\sigma_2}(0)\hat{c}_{\boldsymbol{k}_2 l_3\sigma_2}(0)\right\rangle. \tag{10b}$$

In the RPA level, they are related to the bare susceptibility through the relation

$$\chi^{(\mathrm{s})}(\boldsymbol{q},\mathrm{i}\omega) = \left[I - \chi^{(0)}(\boldsymbol{q},\mathrm{i}\omega)\tilde{U}^{(\mathrm{s})}\right]^{-1}\chi^{(0)}(\boldsymbol{q},\mathrm{i}\omega), \tag{11a}$$

$$\chi^{(\mathrm{c})}(\boldsymbol{q},\mathrm{i}\omega) = \left[I + \chi^{(0)}(\boldsymbol{q},\mathrm{i}\omega)\tilde{U}^{(\mathrm{c})}\right]^{-1}\chi^{(0)}(\boldsymbol{q},\mathrm{i}\omega). \tag{11b}$$

Here, $\chi^{(0)/(\mathrm{s})/(\mathrm{c})}(\boldsymbol{q},\mathrm{i}\omega)$ are the Fourier transformations of $\chi^{(0)/(\mathrm{s})/(\mathrm{c})}(\boldsymbol{q},\tau)$ in the imaginary-frequency space, which are operated as 100×100 matrices by taking the upper and lower two indices as one number, respectively. Note that we only provide the zz-component of the spin susceptibility. In the presence of spin-SU(2) symmetry, the other two components, i.e., the $+-$ and $-+$ components are equal to the zz component. The forms for $\tilde{U}^{(\mathrm{s})/(\mathrm{c})}$ are given in Appendix A.

When $U < U_{\rm c}$, through exchanging short-ranged spin and charge fluctuations between a Cooper pair, an effective pairing interaction vertex $V^{\alpha\beta}(\boldsymbol{k},\boldsymbol{k}')$ will be developed, which leads to the following linearized gap equation near $T_{\rm c}$:

$$-\frac{1}{(2\pi)^2}\sum_\beta \oint_{\rm FS} \mathrm{d}k'_\parallel \frac{V^{\alpha\beta}(\boldsymbol{k},\boldsymbol{k}')}{v^\beta_F(\boldsymbol{k}')}\Delta_\beta(\boldsymbol{k}') = \lambda\Delta_\alpha(\boldsymbol{k}). \tag{12}$$

Here β labels the FS patch, $v^\beta_{\rm F}(\boldsymbol{k}')$ is the Fermi velocity, and $k'_\parallel$ is the tangent component of $\boldsymbol{k}'$. Equation (12) becomes an eigenvalue problem after discretization, with the eigenvector $\Delta_\alpha(\boldsymbol{k})$ representing the gap form factor and the eigenvalue λ determining the corresponding $T_{\rm c}$ through $T_{\rm c} \propto \mathrm{e}^{-1/\lambda}$. From symmetry analysis, each solved $\Delta_\alpha(\boldsymbol{k})$ is attributed to one of the D_3 point-groups for real material with spin-SU(2) symmetry, which corresponds to s, $(\mathrm{p}_x,\mathrm{p}_y)$, $(\mathrm{d}_{x^2-y^2},\mathrm{d}_{xy})$, $\mathrm{f}_{x^3-3xy^2}$, $\mathrm{f}'_{y^3-3yx^2}$, $\mathrm{f}_{x^3-3xy^2}\times\mathrm{f}'_{y^3-3yx^2}$ wave pairings, respectively.

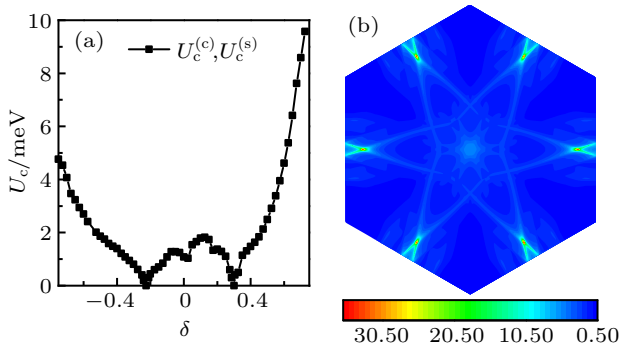


Fig. 3. (a) Doping dependence of $U_{\rm c}^{(\mathrm{s})}$ and $U_{\rm c}^{(\mathrm{c})}$ with $J_{\rm H} = 0$. (b) Distribution of $\chi(\boldsymbol{q})$ for $\delta = -0.2250$ with $J_{\rm H} = 0$ and $U = 0.45$ meV in the Brillouin zone, corresponding to the h-VHS in Fig. 1.

3. Numerical result

In this section, we provide our results of RPA calculations, including the DW orders and leading pairing symmetries. We will first provide the results for the exactly $\mathrm{SU(2)_K \times SU(2)_{K'}}$ symmetric point with $J_{\rm H} = 0$. It will be seen that the CDW and SDW are degenerate, and so are the singlet and triplet SCs. For the realistic material, there would be a tiny symmetry-breaking inter-valley exchange interaction with coefficient $J_{\rm H}$. It would be seen that the results for $J_{\rm H} > 0$ and $J_{\rm H} < 0$ are different although the value of $J_{\rm H}$ is tiny, because of the degeneracy at $J_{\rm H} = 0$.

3.1. The case of $J_{\rm H}=0$

In this subsection, we provide our RPA results for the case of $J_{\rm H}=0$. This condition is an approximation for the realistic material. In this case, the system possesses exact $\mathrm{SU(2)_K}\times\mathrm{SU(2)_{K'}}$ symmetry. It will be seen that this symmetry leads to the degeneracy between the CDW and SDW, and that between singlet SC and triplet one.

The doping dependences of the critical interaction strengths $U_{\rm c}^{(\rm s)}$ and $U_{\rm c}^{(\rm c)}$ are shown in Fig. 3(a). The results show two significant features: (1) Both $U_{\rm c}^{(\rm s)}$ and $U_{\rm c}^{(\rm c)}$ go to zero at the two VH dopings, suggesting that an infinitesimal interaction would drive DW orders at these dopings. This feature originates from the fact that the divergent DOS together with the good FS nesting makes even the bare susceptibility $\chi^{(0)}$ diverge. (2) The $U_{\rm c}^{(\rm s)}$ and $U_{\rm c}^{(\rm c)}$ are exactly equal for a large doping range around the VH dopings, which means that SDW and CDW are degenerate. What is more, the eigenvectors $\xi^{(\rm s)}$ and $\xi^{(\rm c)}$ corresponding to the largest eigenvalues of $\chi^{(\rm s)}(\mathrm{i}\omega=0)$ and $\chi^{(\rm c)}(\mathrm{i}\omega=0)$ are identical too. The origin of this degeneracy will be clarified below.

Due to the $\mathrm{SU(2)_K}\times\mathrm{SU(2)_{K'}}$ symmetry of the MA-TBG in the case of $J_{\rm H}=0$, we can define the unitary symmetry operation $\hat{P}:\hat{c}_i\to\hat{P}\hat{c}_i\hat{P}^\dagger$ as following:

$$\begin{aligned}&\hat{c}_{i\mathrm{K}\iota\uparrow}\to\hat{c}_{i\mathrm{K}\iota\uparrow},\quad \hat{c}_{i\mathrm{K}\iota\downarrow}\to\hat{c}_{i\mathrm{K}\iota\downarrow},\\ &\hat{c}_{i\mathrm{K}'\iota\uparrow}\to\hat{c}_{i\mathrm{K}'\iota\uparrow},\quad \hat{c}_{i\mathrm{K}'\iota\downarrow}\to-\hat{c}_{i\mathrm{K}'\iota\downarrow}.\end{aligned}\tag{13}$$

One can easily check $\left[\hat{P},\,\hat{H}\right]=0$ from Eq. (7) (set $J_{\rm H}=0$) and Eq. (13). A consequence of this symmetry is that it maps an inter-valley CDW order to the z-component of an inter-valley SDW (abbreviated as the z-SDW) one with the same wave vector $\boldsymbol{Q}$ and form factor $\xi(\boldsymbol{Q})$, i.e.,

$$\hat{O}_{\rm CDW}\equiv\sum_{\nu_1\iota_1,\nu_2\iota_2,\boldsymbol{k}\sigma}\hat{c}^\dagger_{\boldsymbol{k}\nu_1\iota_1\sigma}\xi_{\nu_1\iota_1,\nu_2\iota_2}(\boldsymbol{Q})\hat{c}_{\boldsymbol{k}-\boldsymbol{Q}\nu_2\iota_2\sigma},\tag{14a}$$

$$\hat{O}_{z-\rm SDW}\equiv\sum_{\nu_1\iota_1,\nu_2\iota_2,\boldsymbol{k}\sigma\sigma'}\hat{c}^\dagger_{\boldsymbol{k}\nu_1\iota_1\sigma}\xi_{\nu_1\iota_1,\nu_2\iota_2}(\boldsymbol{Q})\sigma^z_{\sigma\sigma'}\hat{c}_{\boldsymbol{k}-\boldsymbol{Q}\nu_2\iota_2\sigma'},\tag{14b}$$

which satisfy

$$\hat{P}^\dagger\hat{O}_{\rm CDW}\hat{P}=\hat{O}_{z-\rm SDW}.\tag{15}$$

Here the inter-valley condition for the DW orders requires

$$\xi_{\nu_1\iota_1,\nu_2\iota_2}=\delta_{\bar{\nu}_1,\nu_2}\xi_{\nu_1\iota_1,\bar{\nu}_1\iota_2}.\tag{16}$$

One can easily check Eq. (15) by using Eqs. (13) and (16).

The above introduced mapping between CDW and collinear SDW here is similar with that for the two-band model adopted in our previous work.[79] The common things of the model studied here and that in our previous work[79] include two aspects. Firstly, the $\mathrm{SU(2)_K}\times\mathrm{SU(2)_{K'}}$ symmetry does not rely on the details of the band structures. Secondly, the inter-valley coherence characters of the DWs in both models originate from the inter-valley FS-nesting character, which is obvious in both models. Then, from this mapping, one can easily prove the degeneracy between the inter-valley CDW and SDW.[79]

The distribution of the largest eigenvalue $\chi(\boldsymbol{q})$ of the bare susceptibility matrix at $\mathrm{i}\omega=0$ in the MBZ is shown in Fig. 3(b) for the h-VH doping. This distribution exhibits a six-folded symmetric pattern peaking at $\pm\boldsymbol{Q}_\alpha$ $(\alpha=1,2,3)$. By comparing with Figs. 2(a) and 2(b), one finds that these $\pm\boldsymbol{Q}_\alpha$ $(\alpha=1,2,3)$ just originate from the FS-nesting vectors shown in Figs. 2(a) and 2(b). In the weak-coupling treatment here, these vectors are just the wave vectors of the DW orders. These wave vectors are near the three M_α-points in the MBZ. Therefore, we have obtained degenerate CDW and SDW orders here, which further hold wave-vector degeneracy. Under such degeneracy between SDW and CDW, as well as the DW orders with different wave vectors, these DW orders would be generally be mixed to lower the ground-state energy. Probably, they would form the chiral SO(4) spin–charge DW order.[79]

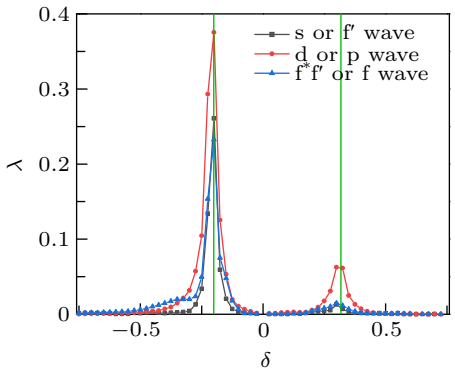


Fig. 4. The largest pairing eigenvalues λ vs. doping for all possible pairing symmetries under $U=0.45$ meV and $J_{\rm H}=0$. Note the degeneracy between the p- and d-, the f′- and s-, and the f- and f*f′-wave pairings, respectively. The degenerate p and d wave pairings dominate over other pairings near the two VH dopings. The two regimes covered with green rectangles represent the DW phase. The insets on both sides show the normalized gap functions for all possible pairing symmetries near the two VH dopings.

The doping-dependences of the largest pairing eigenvalues for all the pairing symmetries are plotted in Fig. 4, where the gap form factors $\Delta_\alpha(\boldsymbol{k})$ (determined by Eq. (12)) near the two VHS points are shown on both sides. The two green rectangles near e-VHS and h-VHS give the regimes for the chiral SO(4) spin–charge DW studied above where $U>U_{\rm c}^{(\rm s)}=U_{\rm c}^{(\rm c)}$, and the remaining regimes support the SC phases. In the regimes near the VHS, the degenerate p- and d-wave pairings are the leading pairing symmetries, while in the over doped regimes far away from the VHS, the degenerate $\mathrm{f}_{x(x^2-3y^2)}$- and $\mathrm{f}_{x(x^2-3y^2)}\times\mathrm{f}'_{y(y^2-3x^2)}$-wave pairings become the leading symmetries. The degeneracy between the singlet and triplet SCs also originates from the above introduced mapping (13), which is a symmetry of the system and can map a singlet pairing to a triplet one.[79]

3.2. The case of $J_H \neq 0$

For realistic material MA-TBG, there always exists a tiny inter-valley exchange interaction with coefficient $J_H \neq 0$, which breaks the exact $SU(2)_K \times SU(2)_{K'}$ symmetry. Because of the degeneracy between the CDW and SDW and that between the singlet and triplet SCs at the exact symmetric point with $J_H = 0$, the tiny $J_H \neq 0$ plays a crucial role to lift up such degeneracies, and singles out the DW or SC which is favored. In the following, we study the case of $J_H \to 0^-$ and $J_H \to 0^+$ separately, with each case adopting $|J_H| = 0.01U$.

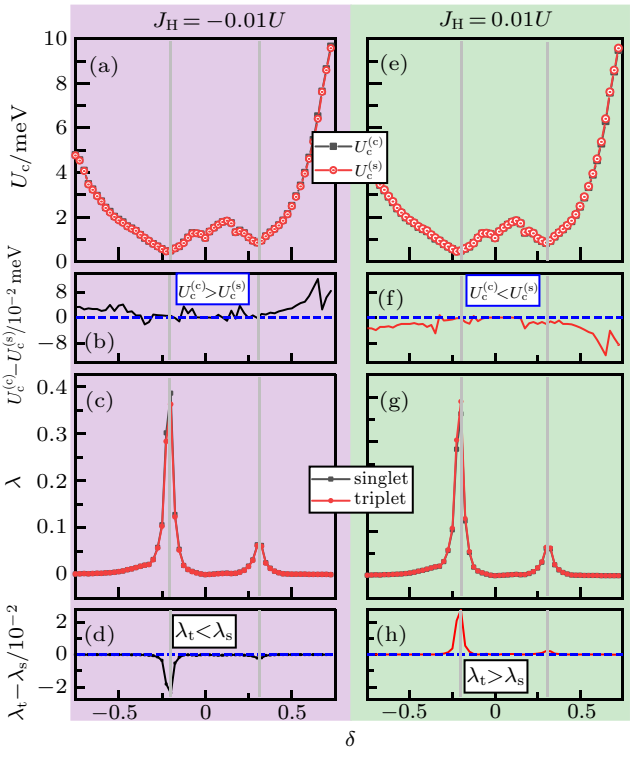


Fig. 5. Doping dependences of $U_c^{(s)}$, $U_c^{(c)}$ (a), (e) and their difference (b), (f) and the largest eigenvalues λ for the singlet-pairing, the triplet pairing (c), (g) and their difference (d), (h) with $J_H = -0.01U$ for the left column and $J_H = 0.01U$ for the right column. In the calculations, $U = 0.45$ meV is adopted.

For the case of $J_H \to 0^-$, we set $J_H = -0.01U$ and redo the RPA calculations. The results of our RPA calculations are shown in Figs. 5(a)–5(d). The doping-dependence of the critical interaction strength $U_c^{(s,c)}$ shown in Fig. 5(a) suggests $U_c^{(c)} > U_c^{(s)}$, as is verified by the broadened $U_c^{(c)} - U_c^{(s)} > 0$ shown in Fig. 5(b). This result suggests that a negative J_H favors the SDW order. A pure chiral SDW ground state would be obtained in this case.[79]

The doping-dependence of the largest pairing eigenvalues for the singlet and triplet pairing symmetries in $J_H \to 0^-$ is shown in Fig. 5(c). Clearly the tiny $SU(2)_K \times SU(2)_{K'}$-symmetry-breaking J_H-term leads to the split between the singlet and triplet pairings. Our results suggest that in this case, the singlet pairings are always favored either near or far away from the VHSs, as shown in Fig. 5(d). Concretely, near the VHS the singlet d-wave pairing wins over the triplet p-wave pairing and becomes the leading pairing symmetry, while far away from the VHS in the over doped regime the singlet $f_{x(x^2-3y^2)} \times f'_{y(y^2-3x^2)}$-wave pairing beats the triplet $f_{x(x^2-3y^2)}$-wave pairing and serves as the leading pairing symmetry. In the experiments reported in Refs. [1,96], the SC is mainly detected near the VHS. Therefore, the experiment-relevant pairing symmetry in the case of $J_H \to 0^-$ should be singlet d-wave pairing. As the d-wave belongs to the 2D irreducible representation, which takes the form of topological $d + id$ pairing state.

The RPA results for $J_H \to 0^+$ are shown in Figs. 5(e)–5(h). Figures 5(e) and 5(f) obviously show $U_c^{(s)} > U_c^{(c)}$, suggesting that the CDW is more favored than the SDW here. However, this does not mean that the ground state for general realistic $U > U_c^{(s)} \approx U_c^{(c)}$ is in the pure CDW phase,[79] due to the wave-vector degeneracy as discussed below. Instead, a nematic DW state with one stripy CDW order mixed with two nematic SDW orders would be obtained to lower the energy.[79]

The doping-dependence of the largest pairing eigenvalues for the singlet and triplet pairing symmetries is shown in Fig. 5(g) for $J_H \to 0^+$. Consequently, the triplet pairings are always favored either near or far away from the VHSs, as shown in Fig. 5(h). Concretely, while the p-wave pairing is favored near the VHS, the $f_{x(x^2-3y^2)}$-wave pairing is the leading symmetry far away from the VHS. The experiment-relevant pairing symmetry near the VH dopings in this case should be triplet p-wave pairing. The degenerate p_x- and p_y-wave pairings would always be mixed into the $p_x \pm ip_y$ form to lower the ground-state energy, i.e., the $p + ip$ for abbreviation, as verified by our numerical results. This state is topologically nontrivial.

4. Discussion and conclusion

In conclusion, we have performed a systematic RPA study on the five-band (per spin and valley) model equipped with extended Hubbard interactions. Due to the inter-valley character of the FS-nesting, the obtained CDW and SDW orders are of inter-valley coherence character. When the tiny inter-valley exchange interaction is neglected, the $SU(2)_K \times SU(2)_{K'}$ symmetry leads to the degeneracy between the CDW and SDW orders, while the D_3 symmetry further causes degeneracy among the DW components with different wave vectors. In such a case, the singlet and triplet SCs have a one-to-one corresponding degeneracy, with the leading pairing symmetry near the VHS to be degenerate $d + id/p + ip$. When the tiny inter-valley exchange interaction is turned on, either SDW or CDW

is favored, determined by the sign of the coefficient of the inter-valley exchange interaction. Similarly, the degeneracy between the $\mathrm{d}+\mathrm{id}$ and $\mathrm{p}+\mathrm{ip}$ is lifted up in such cases. The results obtained here are quite similar with those obtained for the two-band model in our previous study.[79] Such a similarity suggests that the main physics here, including the nature of the correlated insulator and the pairing symmetry, is insensitive to the details of the band structure or the topological aspect near the Dirac nodes. Instead, only the shape of the FS in the doped case and the symmetry of the system would influence the results. This suggests that the two-band model,[80] although blamed for its flaw in the topological aspects, provides a good start point for the study of electron correlations in the MA-TBG in the doped case.

It is important to note that although for $J_{\mathrm{H}} \neq 0$ either SDW or CDW is favored, this does not necessarily suggest that a pure SDW or CDW will be the ground state. Due to the degeneracy between the two DW orders at $J_{\mathrm{H}} = 0$, they would generally be mixed. It is reasonable to conjecture that the mixing will sustain upon a tiny $J_{\mathrm{H}} \neq 0$. In other words, the tiny $J_{\mathrm{H}} \to 0^-$ or $J_{\mathrm{H}} \to 0^+$ just takes the role of determining the mixing manner between the two DW orders, instead of choosing one. Further more, the wave-vector degeneracy caused by the D_3 symmetry will play an important role in determining the mixing manner. Actually, as predicted in our previous study,[79] the SDW and CDW will be mixed into the chiral SO(4) spin–charge DW state, which simultaneously hosts three 4-component vectorial DW order parameters with each of them taking a wave vector $\boldsymbol{Q}_\alpha$. The polarization directions of the three 4-vectorial DW order parameters are mutually perpendicular to one another and can globally rotate in the $\mathbb{R}^4$ space without costing energy. The role of the tiny J_{H} is to pin down to some extent the polarization directions of the three 4-vectorial DW order parameters. As a result, for $J_{\mathrm{H}} \to 0^-$ where the SDW is favored, the CDW axis in the $\mathbb{R}^4$ space becomes the "difficult" axis, and all of the three 4-vectorial DW order parameters will avoid the CDW axis and take the SDW axes, leading to a pure chiral SDW state. On the contrary, for $J_{\mathrm{H}} \to 0^+$ where the CDW is favored, the CDW axis in the $\mathbb{R}^4$ space becomes the "easy" axis, and all of the three mutually perpendicular 4-vectorial DW order parameters compete to take this axis. However, at most one lucky DW order parameter is given the opportunity to point along the CDW axis, with the remaining two stays in the SDW space. Further more, it is random on which wave vector is distributed to the CDW order parameter, leading to a nematic DW phase, consistent with recent STM experiments.[97,98] Such a point of view is different from that held in Refs. [47,68]. The mean-field calculations for this part will be left for future study.

Note that starting from the ten-band TB model here without really constructing the Wannier states, we actually do not know the accurate form of the interaction part of the Hamiltonian, as well as the coefficient of each term. Here we only take a simple Hubbard–Hund type of interaction. A first-principle based calculation is needed to get the more quantitative description of the interaction part. However, most probably, the conclusions obtained here might not be changed, as all the main physics obtained here is simply based on the symmetry of the system, which does not rely on the details of the interactions. We leave such study for the future.

Appendix A: More information on RPA approach

In this appendix, we provide the explicit form of the non-interaction susceptibility $\chi^{(0)}$, the interaction matrices $\tilde{U}^{(\mathrm{s})}$ and $\tilde{U}^{(\mathrm{c})}$, and the effective pairing interaction vertex $V^{\alpha\beta}(\boldsymbol{k},\boldsymbol{k}')$.

The form of $\chi^{(0)}$ is given by

$$\chi^{(0)l_1l_2}_{l_3l_4}(\boldsymbol{q},\mathrm{i}\omega) = \frac{1}{N}\sum_{\boldsymbol{k},\alpha\beta}\frac{n_{\mathrm{F}}(\varepsilon^{\beta}_{\boldsymbol{k}+\boldsymbol{q}}) - n_{\mathrm{F}}(\varepsilon^{\alpha}_{\boldsymbol{k}})}{\varepsilon^{\alpha}_{\boldsymbol{k}} - \varepsilon^{\beta}_{\boldsymbol{k}+\boldsymbol{q}} + \mathrm{i}\omega} \times \xi^{\alpha *}_{l_1}(\boldsymbol{k})\xi^{\beta}_{l_2}(\boldsymbol{k}+\boldsymbol{q})\xi^{\beta *}_{l_4}(\boldsymbol{k}+\boldsymbol{q})\xi^{\alpha}_{l_3}(\boldsymbol{k}), \quad \text{(A1)}$$

where $n_{\mathrm{F}}(\varepsilon^{\alpha}_{\boldsymbol{k}})$ is the Fermi distribution. α and β represent the the combined index $(\iota_1\nu_1,\iota_2\nu_2)$ in Eq. (6). $\varepsilon^{\alpha}_{\boldsymbol{k}}$ and $\xi^{\alpha}(\boldsymbol{k})$ are the energy level and the corresponding eigenstate at the wave vector $\boldsymbol{k}$ for the α-th band. In the RPA level, the renormalized spin and charge susceptibilities have been given in Eqs. (11a) and (11(b)).

Labelling orbitals

$$\left\{\tau_{\mathrm{p_z};+},\tau_{\mathrm{p_+};+},\tau_{\mathrm{p_-};+},\eta^{(\mathrm{A})}_{\mathrm{s};+},\eta^{(\mathrm{B})}_{\mathrm{s};+},\tau_{\mathrm{p_z};-},\tau_{\mathrm{p_+};-},\tau_{\mathrm{p_-};-},\eta^{(\mathrm{A})}_{\mathrm{s};-},\eta^{(\mathrm{B})}_{\mathrm{s};-},\right\}$$

as $\{1,2,3,\ldots,9,10\}$, the first five indicators are at K valley, the last five indicators are at K′ valley, which have been distinguished by positive and negative signs. The explicit forms of $U^{(\mathrm{s})}$ and $U^{(\mathrm{c})}$ are given as follows:

$$U^{(\mathrm{s})l_1l_2}_{l_3l_4} = \begin{cases} U, & l_1=l_2=l_3=l_4 \in [1,2,3,6,7,8], \\ U, & l_1=l_4\neq l_2=l_3 \in [1,2,3,6,7,8], \\ U', & l_1=l_2=l_3=l_4 \in [4,5,9,10], \\ -J_{\mathrm{H}}, & l_1=l_2=\bar{l}_3=\bar{l}_4 \in [1,2,3,6,7,8], \\ U', & l_1=\bar{l}_2=l_3=\bar{l}_4 \in [4,5,9,10], \end{cases} \quad \text{(A2)}$$

$$U^{(\mathrm{c})l_1l_2}_{l_3l_4}=\begin{cases}U, & l_1=l_2=l_3=l_4\in[1,2,3,6,7,8],\\ 2U, & l_1=l_2\neq l_3=l_4\in[1,2,3,6,7,8],\\ -U-2J_{\mathrm{H}}\delta_{l_1\bar{l}_2l_3\bar{l}_4}, & l_1=l_4\neq l_2=l_3\in[1,2,3,6,7,8],\\ U', & l_1=l_2=l_3=l_4\in[4,5,9,10],\\ \tilde{W}(\boldsymbol{q},l_1,l_2,l_3,l_4), & l_1=l_2<l_3=l_4\in[4,5,9,10],\\ \tilde{W}^{\dagger}(\boldsymbol{q},l_1,l_2,l_3,l_4), & l_1=l_2>l_3=l_4\in[4,5,9,10],\\ 2U', & l_1=l_2=\bar{l}_3=\bar{l}_4\in[4,5,9,10],\\ -U', & l_1=\bar{l}_2=\bar{l}_3=l_4\in[4,5,9,10].\end{cases}\tag{A3}$$

In the expressions of $U^{(\mathrm{c})}$, $\tilde{W}(\boldsymbol{q},l_1,l_2,l_3,l_4)=2W\left(1+\mathrm{e}^{\mathrm{i}q_1}+\mathrm{e}^{-\mathrm{i}q_2}\right)(1-\delta_{l_1\bar{l}_3})$, $q_{1,2}\equiv\boldsymbol{q}\cdot\boldsymbol{a}_{1,2}$, where $\boldsymbol{a}_{1,2}$ are the two unit vectors of the Moiré lattice.

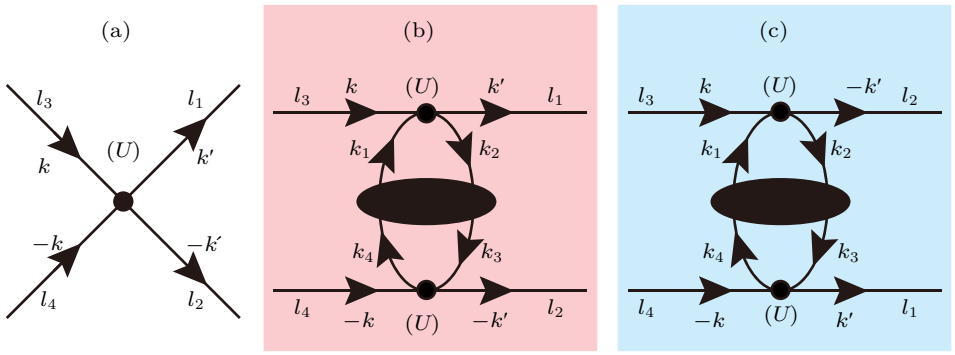


Fig. A1. Three processes that have contributions to the renormalized effective vertex in the RPA: (a) bare interaction vertex and (b), (c) two second order perturbation processes during which spin or charge fluctuations are exchanged within a cooper pair.

In the RPA level, the Cooper pair with momentum and orbital of $(\boldsymbol{k}l_3,-\boldsymbol{k}l_4)$ could be scattered into $(\boldsymbol{k}'l_1,-\boldsymbol{k}'l_2)$ by exchanging charge or spin fluctuations, see Fig. A1 which is up to the second order perturbation processes. This process induces the following effective interaction:

$$V_{\mathrm{eff}}=\frac{1}{N}\sum_{\alpha\beta,\boldsymbol{k}\boldsymbol{k}'}V^{\alpha\beta}(\boldsymbol{k},k')\hat{c}^{\dagger}_{\boldsymbol{k}\alpha}\hat{c}_{\bar{\boldsymbol{k}}\bar{\alpha}}\hat{c}^{\dagger}_{\bar{\boldsymbol{k}}'\bar{\beta}}\hat{c}_{\boldsymbol{k}'\beta},\tag{A4}$$

where $\bar{\alpha}$ and $\bar{\beta}$ denote the opposite-valley bands of the α-th and β-th ones, respectively, and $\bar{\boldsymbol{k}}=\boldsymbol{k}$. The effective pairing interaction vertex $V^{\alpha\beta}(\boldsymbol{k},k')$ has the form

$$\begin{aligned}V^{\alpha\beta}(\boldsymbol{k},k')=&\sum_{l_1l_2l_3l_4}\Gamma^{l_1l_2}_{l_3l_4}(\boldsymbol{k},k',0)\xi^{\alpha,*}_{l_1}(\boldsymbol{k})\xi^{\bar{\alpha},*}_{l_2}\\&\times(-\boldsymbol{k})\xi^{\bar{\beta}}_{l_4}(-\boldsymbol{k}')\xi^{\beta}_{l_3}(\boldsymbol{k}').\end{aligned}\tag{A5}$$

The three processes that have contributions to $\Gamma^{l_1l_2}_{l_4l_3}(\boldsymbol{k},\boldsymbol{k}')$ are presented in Fig. A1 where (a) denotes the bare interaction vertex and (b), (c) represent two second order perturbation processes, during which the spin or charge fluctuations are exchanged within a cooper pair. The effective vertex $\Gamma^{l_1l_2}_{l_3l_4}(\boldsymbol{k},\boldsymbol{k}')$ is

$$\begin{aligned}&\Gamma^{(\mathrm{s})l_1l_2}_{l_3l_4}(\boldsymbol{k},\boldsymbol{k}')\\&=\left(\frac{U^{(\mathrm{c})}(\boldsymbol{k}-\boldsymbol{k}')+U^{(\mathrm{s})}}{4}\right)^{l_1l_3}_{l_2l_4}+\left(\frac{U^{(\mathrm{c})}(\boldsymbol{k}+\boldsymbol{k}')+U^{(\mathrm{s})}}{4}\right)^{l_1l_4}_{l_2l_3}\\&+\frac{1}{4}\left[3U^{(\mathrm{s})}\chi^{(\mathrm{s})}\left(\boldsymbol{k}-\boldsymbol{k}'\right)U^{(\mathrm{s})}-U^{(\mathrm{c})}\chi^{(\mathrm{c})}\left(\boldsymbol{k}-\boldsymbol{k}'\right)U^{(\mathrm{c})}\right]^{l_1l_3}_{l_2l_4}\\&+\frac{1}{4}\left[3U^{(\mathrm{s})}\chi^{(\mathrm{s})}\left(\boldsymbol{k}+\boldsymbol{k}'\right)U^{(\mathrm{s})}-U^{(\mathrm{c})}\chi^{(\mathrm{c})}\left(\boldsymbol{k}+\boldsymbol{k}'\right)U^{(\mathrm{c})}\right]^{l_1l_4}_{l_2l_3}\end{aligned}\tag{A6}$$

for the singlet channel, and is

$$\begin{aligned}&\Gamma^{(t)l_1l_2}_{l_3l_4}(\boldsymbol{k},\boldsymbol{k}')\\&=\left(\frac{U^{(\mathrm{c})}(\boldsymbol{k}-\boldsymbol{k}')+U^{(\mathrm{s})}}{4}\right)^{l_1l_3}_{l_2l_4}-\left(\frac{U^{(\mathrm{c})}(\boldsymbol{k}+\boldsymbol{k}')+U^{(\mathrm{s})}}{4}\right)^{l_1l_4}_{l_2l_3}\\&+\frac{1}{4}\left[U^{(\mathrm{s})}\chi^{(\mathrm{s})}\left(\boldsymbol{k}-\boldsymbol{k}'\right)U^{(\mathrm{s})}+U^{(\mathrm{c})}\chi^{(\mathrm{c})}\left(\boldsymbol{k}-\boldsymbol{k}'\right)U^{(\mathrm{c})}\right]^{l_1l_3}_{l_2l_4}\\&+\frac{1}{4}\left[U^{(\mathrm{s})}\chi^{(\mathrm{s})}\left(\boldsymbol{k}+\boldsymbol{k}'\right)U^{(\mathrm{s})}+U^{(\mathrm{c})}\chi^{(\mathrm{c})}\left(\boldsymbol{k}+\boldsymbol{k}'\right)U^{(\mathrm{c})}\right]^{l_1l_4}_{l_2l_3}\end{aligned}\tag{A7}$$

for the triplet channel. Note that the vertex $\Gamma^{l_1l_2}_{l_3l_4}(\boldsymbol{k},\boldsymbol{k}')$ has been symmetrized and anti-symmetrized for the singlet and triplet cases, respectively. The vertex $\Gamma^{l_1l_2}_{l_3l_4}(\boldsymbol{k},\boldsymbol{k}')$ gives the effective paring interaction vertex $V^{\alpha\beta}(\boldsymbol{k},k')$.

References

[1] Cao Y, Fatemi V, Demir A, Fang S, Tomarken S L, Luo J Y, Sanchez-Yamagishi J D, Watanabe K, Taniguchi T, Kaxiras E C, Ashoori R and Jarillo-Herrero P 2018 *Nature* **556** 80

[2] Cao Y, Fatemi V, Fang S, Watanabe K, Taniguchi T, Kaxiras E and Jarillo-Herrero P 2018 *Nature* **556** 43

[3] Bistritzer R and MacDonald A H 2011 *Proc. Natl. Acad. Sci. USA* **108** 12233

[4] Dos Santos J L, Peres N and Neto A C 2007 *Phys. Rev. Lett.* **99** 256802

[5] Chittari B L, Chen G, Zhang Y, Wang F and Jung J 2019 *Phys. Rev. Lett.* **122** 016401

[6] Wu F, Lovorn T, Tutuc E and MacDonald A H 2018 *Phys. Rev. Lett.* **121** 026402

[7] Xian L, Kennes D M, Tancogne-Dejean N, Altarelli M and Rubio A 2019 *Nano Lett.* **19** 4934
[8] Tomarken S, Cao Y, Demir A, Watanabe K, Taniguchi T, Jarillo-Herrero P and Ashoori R 2019 *Phys. Rev. Lett.* **123** 046601
[9] Liao Y D, Meng Z Y and Xu X Y 2019 *Phys. Rev. Lett.* **123** 157601
[10] Hu X, Hyart T, Pikulin D I and Rossi E 2019 *Phys. Rev. Lett.* **123** 237002
[11] Yudhistira I, Chakraborty N, Sharma G, Ho D Y, Laksono E, Sushkov O P, Vignale G and Adam S 2019 *Phys. Rev. B* **99** 140302
[12] Padhi B and Phillips P W 2019 *Phys. Rev. B* **99** 205141
[13] Ramires A and Lado J L 2019 *Phys. Rev. B* **99** 245118
[14] Schrade C and Fu L 2019 *Phys. Rev. B* **100** 035413
[15] Bi Z, Yuan N F Q and Fu L 2019 *Phys. Rev. B* **100** 035448
[16] Lin Y P and Nandkishore R M 2019 *Phys. Rev. B* **100** 085136
[17] Klebl L and Honerkamp C 2019 *Phys. Rev. B* **100** 155145
[18] Pizarro J, Rösner M, Thomale R, Valentí R and Wehling T 2019 *Phys. Rev. B* **100** 161102
[19] Goodwin Z A, Corsetti F, Mostofi A A and Lischner J 2019 *Phys. Rev. B* **100** 235424
[20] Zhu Z, Sheng D and Fu L 2019 *Phys. Rev. Lett.* **123** 087602
[21] Wu X C, Jian C M and Xu C 2019 *Phys. Rev. B* **99** 161405
[22] Goodwin Z A, Corsetti F, Mostofi A A and Lischner J 2019 *Phys. Rev. B* **100** 121106
[23] Venderbos J W and Fernandes R M 2018 *Phys. Rev. B* **98** 245103
[24] Haule M, Andrei E and Haule K 2019 arXiv:1901.09852
[25] Kang J and Vafek O 2018 *Phys. Rev. X* **8** 031088
[26] Kang J and Vafek O 2019 *Phys. Rev. Lett.* **122** 246401
[27] Xu X Y, Law K T and Lee P A 2018 *Phys. Rev. B* **98** 121406
[28] Padhi B, Setty C and Phillips P W 2018 *Nano Lett.* **18** 6175
[29] Pizarro J, Calderón M and Bascones E 2019 *J. Phys. Commun.* **3** 035024
[30] Thomson A, Chatterjee S, Sachdev S and Scheurer M S 2018 *Phys. Rev. B* **98** 075109
[31] Zhang Y H, Mao D, Cao Y, Jarillo-Herrero P and Senthil T 2019 *Phys. Rev. B* **99** 075127
[32] Liu J, Liu J and Dai X 2019 *Phys. Rev. B* **99** 155415
[33] Xie M and MacDonald A H 2020 *Phys. Rev. Lett.* **124** 097601
[34] Wu X C, Keselman A, Jian C M, Pawlak K A and Xu C 2019 *Phys. Rev. B* **100** 024421
[35] Yuan N F Q and Fu L 2018 *Phys. Rev. B* **98** 045103
[36] Codecido E, Wang Q, Koester R, Che S, Tian H, Lv R, Tran S, Watanabe K, Taniguchi T, Zhang F, Bockrath M and Ning Lau C 2019 *Sci. Adv.* **5** EAAW9770
[37] Dodaro J F, Kivelson S A, Schattner Y, Sun X Q and Wang C 2018 *Phys. Rev. B* **98** 075154
[38] Liu C C, Zhang L D, Chen W Q and Yang F 2018 *Phys. Rev. Lett.* **121** 217001
[39] Fidrysiak M, Zegrodnik M and Spałek J 2018 *Phys. Rev. B* **98** 085436
[40] Guo H M, Zhu X, Feng S P and Scalettar R T 2018 *Phys. Rev. B* **97** 235453
[41] Ochi M, Koshino M and Kuroki K 2018 *Phys. Rev. B* **98** 081102
[42] Lu X, Stepanov P, Yang W, Xie M, Aamir M A, Das I, Urgell C, Watanabe K, Taniguchi T, Zhang G, Bachtold A H, MacDonald A and Efetov D K 2019 *Nature* **574** 653
[43] Huang T, Zhang L and Ma T X 2019 *Sci. Bull.* **64** 310
[44] Rademaker L and Mellado P 2018 *Phys. Rev. B* **98** 235158
[45] Classen L, Honerkamp C and Scherer M M 2019 *Phys. Rev. B* **99** 195120
[46] Kennes D M, Lischner J and Karrasch C 2018 *Phys. Rev. B* **98** 241407
[47] Isobe H, Yuan N F and Fu L 2018 *Phys. Rev. X* **8** 041041
[48] Sherkunov Y and Betouras J J 2018 *Phys. Rev. B* **98** 205151
[49] Xu C and Balents L 2018 *Phys. Rev. Lett.* **121** 087001
[50] Roy B and Juričić V 2019 *Phys. Rev. B* **99** 121407
[51] Zhang L 2019 *Sci. Bull.* **64** 495
[52] Ray S, Jung J and Das T 2019 *Phys. Rev. B* **99** 134515
[53] Su Y and Lin S Z 2018 *Phys. Rev. B* **98** 195101
[54] Peltonen T J, Ojajärvi R and Heikkilä T T 2018 *Phys. Rev. B* **98** 220504
[55] Wu F, MacDonald A and Martin I 2018 *Phys. Rev. Lett.* **121** 257001
[56] Lian B, Wang Z and Bernevig B A 2019 *Phys. Rev. Lett.* **122** 257002
[57] Zhang L, Huang T, Liang Y and Ma T 2020 *Mode. Phys. Lett. B* **34** 2050016
[58] Brydon P, Abergel D S, Agterberg D and Yakovenko V M 2019 *Phys. Rev. X* **9** 031025
[59] Angeli M, Tosatti E and Fabrizio M 2019 *Phys. Rev. X* **9** 041010
[60] Tang Q K, Yang L, Wang D, Zhang F C and Wang Q H 2019 *Phys. Rev. B* **99** 094521
[61] Alidoust M, Willatzen M and Jauho A P 2019 *Phys. Rev. B* **99** 155413
[62] Wu F 2019 *Phys. Rev. B* **99** 195114
[63] Wu F and Sarma S D 2019 *Phys. Rev. B* **99** 220507
[64] Wang J, Mu X, Wang L and Sun M 2019 *Mater. Today Phys.* **9** 100099
[65] Chen L, Li H Z and Han R S 2018 *J. Phys.: Cond. Matter.* **31** 065601
[66] Liu Z, Li Y and Yang Y f 2019 *Chin. Phys. B* **28** 077103
[67] Choi Y W and Choi H J 2018 *Phys. Rev. B* **98** 241412
[68] You Y Z and Vishwanath A 2019 *NPJ Quantum Materials* **4** 1
[69] Gonzalez J and Stauber T 2019 *Phys. Rev. Lett.* **122** 026801
[70] Laksono E, Leaw J N, Reaves A, Singh M, Wang X, Adam S and Gu X 2018 *Solid State Commun.* **282** 38
[71] Wu F, Hwang E and Sarma S D 2019 *Phys. Rev. B* **99** 165112
[72] Fang S C, Liu G K, Lin H Q and Huang Z B 2019 *Phys. Rev. B* **100** 115135
[73] Wu X, Hanke W, Fink M, Klett M and Thomale R 2020 *Phys. Rev. B* **101** 134517
[74] Lin Y P and Nandkishore R M 2018 *Phys. Rev. B* **98** 214521
[75] Kozii V, Isobe H, Venderbos J W and Fu L 2019 *Phys. Rev. B* **99** 144507
[76] Yuan N F, Isobe H and Fu L 2019 *Nat. Commun.* **10** 1
[77] Cea T, Walet N R and Guinea F 2019 *Phys. Rev. B* **100** 205113
[78] Harshman D R and Fiory A T 2020 *J. Supercond. Nov. Magn.* **33** 367
[79] Lu C, Zhang Y, Zhang Y, Zhang M, Liu C C, Gu Z C, Chen W Q and Yang F 2020 arXiv:2003.09513
[80] Koshino M, Yuan N F, Koretsune T, Ochi M, Kuroki K and Fu L 2018 *Phys. Rev. X* **8** 031087
[81] Po H C, Zou L, Senthil T and Vishwanath A 2019 *Phys. Rev. B* **99** 195455
[82] Zhou J H, Qin T and Shi J R 2013 *Chin. Phys. Lett.* **30** 017401
[83] Po H C, Zou L, Vishwanath A and Senthil T 2018 *Phys. Rev. X* **8** 031089
[84] Bistritzer R and MacDonald A H 2010 *Phys. Rev. B* **81** 245412
[85] Lee J Y, Khalaf E, Liu S, Liu X, Hao Z, Kim P and Vishwanath A 2019 *Nat. Commun.* **10** 1
[86] Takimoto T, Hotta T and Ueda K 2004 *Phys. Rev. B* **69** 104504
[87] Yada K and Kontani H 2005 *J. Phys. Soc. Japan* **74** 2161
[88] Kubo K 2007 *Phys. Rev. B* **75** 224509
[89] Kuroki K, Onari S, Arita R, Usui H, Tanaka Y, Kontani H and Aoki H 2008 *Phys. Rev. Lett.* **101** 087004
[90] Graser S, Maier T, Hirschfeld P and Scalapino D 2009 *New J. Phys.* **11** 025016
[91] Maier T, Graser S, Hirschfeld P and Scalapino D 2011 *Phys. Rev. B* **83** 100515
[92] Liu F, Liu C C, Wu K, Yang F and Yao Y 2013 *Phys. Rev. Lett.* **111** 066804
[93] Wu X, Yuan J, Liang Y, Fan H and Hu J 2014 *Europhys. Lett.* **108** 27006
[94] Ma T, Yang F, Yao H and Lin H Q 2014 *Phys. Rev. B* **90** 245114
[95] Zhang L D, Yang F and Yao Y 2015 *Sci. Rep.* **5** 8203
[96] Yankowitz M, Chen S, Polshyn H, Zhang Y, Watanabe K, Taniguchi T, Graf D, Young A F and Dean C R 2019 *Science* **363** 1059
[97] Jiang Y, Lai X, Watanabe K, Taniguchi T, Haule K, Mao J and Andrei E Y 2019 *Nature* **573** 91
[98] Kerelsky A, McGilly L J, Kennes D M, Xian L, Yankowitz M, Chen S, Watanabe K, Taniguchi T, Hone J, Dean C, Rubio A and Pasupathy A N 2019 *Nature* **572** 95